Journal of Hazardous Materials 192 (2011) 208–221

Contents lists available at ScienceDirect

Journal of Hazardous Materials

journal homepage: www.elsevier.com/locate/jhazmat

Development of graded Ni–YSZ composite coating on Alloy 690 by Pulsed Laser Deposition technique to reduce hazardous metallic nuclear waste inventory

Pranesh Sengupta[a,b,*], Detlef Rogalla[c], Hans Werner Becker[d], Gautam Kumar Dey[a], Sumit Chakraborty[b]

[a] Materials Science Division, Bhabha Atomic Research Centre, Mumbai 400 085, India
[b] Institut für Geologie, Mineralogie und Geophysik, Ruhr Universität Bochum, Bochum D-44780, Germany
[c] RUBION, Ruhr Universität Bochum, Bochum D-44780, Germany
[d] Fakultät für Physik und Astronomie, Ruhr Universität Bochum, Bochum D-44780, Germany

ARTICLE INFO

Article history:
Received 5 February 2011
Received in revised form 9 April 2011
Accepted 2 May 2011
Available online 2 June 2011

Keywords:
Hazardous metallic nuclear waste
Alloy 690
High-level waste vitrification furnace
Ni–YSZ composite coating
Pulsed Laser Deposition technique

ABSTRACT

Alloy 690 based 'nuclear waste vitrification furnace' components degrade prematurely due to molten glass–alloy interactions at high temperatures and thereby increase the volume of metallic nuclear waste. In order to reduce the waste inventory, compositionally graded Ni–YSZ (Y_2O_3 stabilized ZrO_2) composite coating has been developed on Alloy 690 using Pulsed Laser Deposition technique. Five different thin-films starting with Ni80YSZ20 (Ni 80 wt% + YSZ 20 wt%), through Ni60YSZ40 (Ni 60 wt% + YSZ 40 wt%), Ni40YSZ60 (Ni 40 wt% + YSZ 60 wt%), Ni20YSZ80 (Ni 20 wt% + YSZ 80 wt%) and Ni0YSZ100 (Ni 0 wt% + YSZ 100 wt%), were deposited successively on Alloy 690 coupons. Detailed analyses of the thin-films identify them as homogeneous, uniform, pore free and crystalline in nature. A comparative study of coated and uncoated Alloy 690 coupons, exposed to sodium borosilicate melt at 1000 °C for 1–6 h suggests that the graded composite coating could substantially reduced the chemical interactions between Alloy 690 and borosilicate melt.

1. Introduction

Vitrification of high level nuclear waste (HLW) is considered to be one of the best available immobilization options today [1–5]. The basic idea behind the process is to produce suitable borosilicate waste glass matrices capable of hosting hazardous radionuclides in geological repositories for a minimum period of 10^4–10^6 years. Various types of vitrification processes have been suggested in the literature [6,7], but the ones which are most commonly followed at the Waste Immobilization Plant scale, are (a) induction heated metallic melter pot and (b) Joule heated ceramic melter pot. The success of a vitrification technique is of course assessed by the quality of nuclear waste glass produced, but it also depends on the length of uninterrupted service it can provide. Faster degradation or pre-mature failure of melter pot materials, especially components made up of nickel (Ni) based austenitic Superalloy 690 (e.g. thermowells, feeders, electrodes, pour spout assemblies, metallic process pot, etc.), have been identified as one of the main reasons behind the unprecedented shut down of vitrification plant operations. To avoid such situations it is absolutely necessary to understand and prevent such failures as much as possible. Towards this, Sengupta and his co-workers have carried out a significant number of experimental studies under partially simulated service conditions [8–14] and they have reported the following physico-chemical changes at the Alloy 690/sodium barium borosilicate melt interfaces (Fig. 1(a) and (b)),

(i) secondary Cr carbide ($Cr_{23}C_6$ type) precipitation along grain boundaries and at triple point junctions (mostly free from TiN particles) within the alloy,
(ii) Cr depletion in austenitic matrix,
(iii) intergranular attack within the alloy,
(iv) formation of Cr_2O_3 and glassy layers (containing needle shaped Ni_2CrO_4, and cubic $NiCr_2O_4$ phases) at the Alloy 690–waste glass interface,
(v) segregation of heat producing and β–γ emitting radionuclides, e.g. ^{90}Sr and ^{137}Cs within the glassy layer from the waste glass melt pool, and
(vi) incorporation of waste glass melt pool components including radionuclides within corroded Alloy 690 through diffusion and redistribution along intergralunar cracks, etc.

Although this is the general reaction trend at the interface, the nature and the extent of the reaction(s) may change at different

* Corresponding author at: Materials Science Division, Bhabha Atomic Research Centre, Mumbai, Maharashtra 400 085, India. Tel.: +91 22 2559 0468; fax: +91 22 2550 5151.
E-mail address: praneshsengupta@gmail.com (P. Sengupta).

0304-3894/$ – see front matter © 2011 Elsevier B.V. All rights reserved.
doi:10.1016/j.jhazmat.2011.05.006

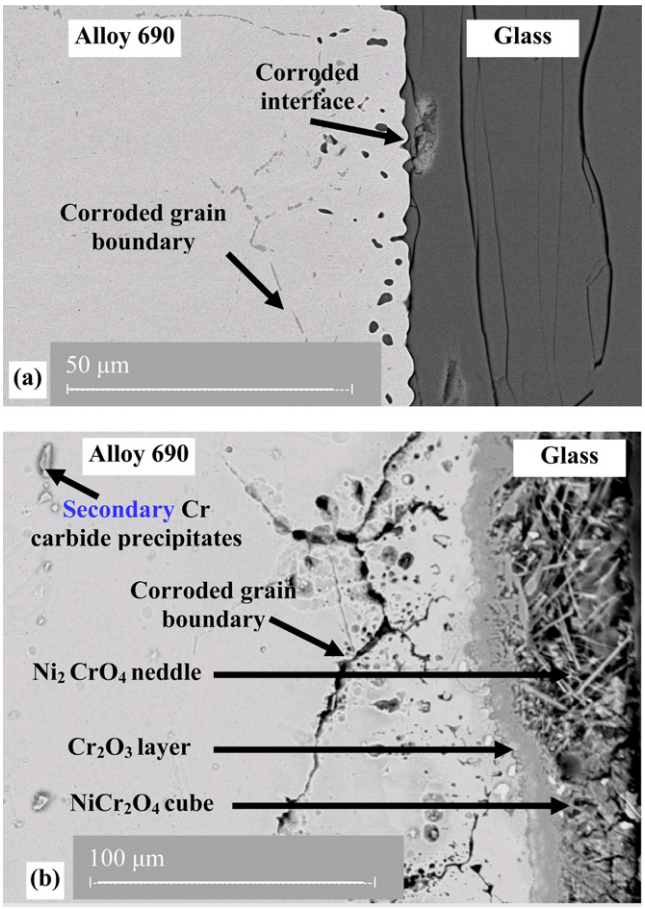

Fig. 1. BSE images showing the physico-chemical modifications within Alloy 690 coupons upon exposure to sodium barium borosilicate glass melt at 950 °C for (a) 2 h and (b) 144 h.

locations within a given type of vitrification furnace or with the change in furnace type or process flow sheet, as the adjacent service conditions (temperature, fugacity of oxygen (f_{O2}), time of interaction, viscosity, chemical composition of adjacent fluid phase(s), relative dominance of liquid or gaseous phases, stress, etc.) are very different in each case [15,16].

All these microstructural–microchemical changes at the Alloy 690–waste glass melt pool not only deteriorate waste glass properties but also significantly degrade the metallurgical properties of the alloy. This becomes evident with the (i) formation of pores within the melter pot wall and pour spout assembly, (ii) cracking and/or bending of electrode, melter pot, etc. Usually rise in radioactivity within the hot cell and multiple pouring of waste glass melt in place of pencil pouring indicates the failure of a vitrification furnace. Failed Alloy 690 components so obtained retain significant amount of radioactivity with it due to presence of adhering glassy layer on its surface and incorporation of waste glass components within it. Earlier attempts to dissolve the glassy layer with concentrated mixed acids remained unsuccessful due to the inert nature of the former. Moreover, reduction of metallic nuclear waste volume through mechanical shearing or otherwise, was also not possible due to enhanced toughness of the alloy because of grain growth upon thermal annealing. Thus, as of today, the required scientific knowledge base as well as remote-robot based technology is not available for disposal of metallic nuclear waste. Hence the failed Alloy 690 components remain to be a serious threat for human and associated biosphere.

To address this issue there are two options available, (a) identification of an alternative for Alloy 690 or (b) developing 'chemical diffusion barrier coating' for it. Among these two, the first option is preferred, but since it takes time to develop a new Superalloy so the immediate remedy should be to develop suitable coating materials. Considering the harsh environment within vitrification furnaces it is prudent to explore ceramic coatings because this approach has been routinely successful in chemical industries to combat material degradations. For selection of the coating material and optimization of its processing route we have taken a multidisciplinary approach where we used experience gained from previous experimental studies to meet our objective. Brief notes on each of these aspects are described below.

2. The qualifying criteria for chemical diffusion barrier coating

Understanding the service conditions is very crucial for identifying and developing any chemical diffusion barrier coating material. Usually the HLWs are 1.5–3.0 M HNO_3 solutions containing radioisotopes of as many as 30–40 different elements belonging to different categories such as (i) fission products, (ii) activation products, (iii) chemical additives, (iv) actinides, and (v) minor actinides. The vitrification process generally takes place at high temperature, close to 950–1000 °C, which leads to evaporation and concentration of HNO_3 and hence of HLW. Therefore the environment within vitrification furnaces is usually very aggressive due to

(i) presence of multiple elements in different ionic states,
(ii) different orders of radioactivity and toxicity associated with these isotopes/ionic species,
(iii) high temperature operation,
(iv) high acidic environment,
(v) high oxygen fugacity, etc.

Moreover vitrification process involves considerable convective motion within borosilicate melt which makes the environment even more complicated.

Considering all these factors, the qualifying criteria any potential chemical diffusion barrier material has to satisfy, are the following:

(i) the material should be able to arrest elemental exchange between Alloy 690 and adjacent HLW loaded borosilicate melt,
(ii) the material should be compatible with Cr and Cr oxides, adjacent silicate melts as well as acidic waste solutions containing radioactive and toxic elements,
(iii) the material should be stable under high temperature and high f_{O2} environment,
(iv) it should be able to withstand the thermal shocks associated with batch scale productions,
(v) it should act as element diffusion barrier and not as a thermal barrier, and
(vi) the required coating technology should be already available.

3. Selection of the coating material

Given the above mentioned service conditions and requirements, ceramic coatings appear to be the most promising diffusion barrier material in the present case. Available experimental data together with plant scale experiences acquired over the last few decades identify Al_2O_3 and YSZ (ZrO_2 with 8 mol% Y_2O_3) as the two most promising diffusion barrier coating materials for the present case [17]. It is noted that both the materials have excellent thermal, mechanical and chemical properties, and could be emplaced on Ni based alloys following plasma spray coating routes (air

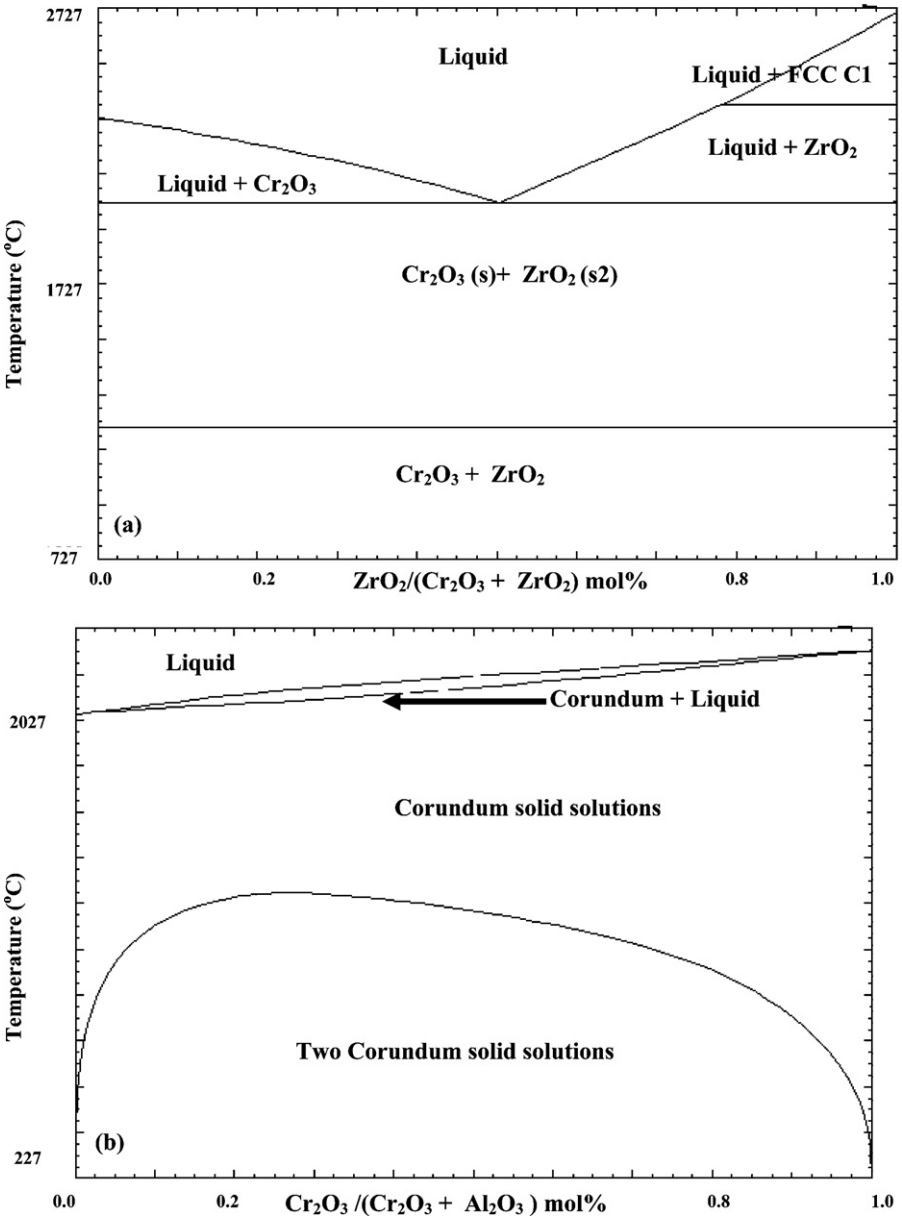

Fig. 2. Selected phase diagrams important for present study [22–24].

plasma spray, thermal plasma spray, vacuum plasma spray, small particle plasma spray processing, high velocity oxy-fuel process, etc.), electron beam physical vapor deposition technique, dip coating, sol–gel, aluminizing process, slurry coating, etc. [17–21]. However, available X-Cr_2O_3 (where X: Al_2O_3, ZrO_2) phase diagrams (Fig. 2(a) and (b) [22,23]) show Cr_2O_3 is more compatible with Al_2O_3 (forms solid solution) than YSZ. On the other hand, YSZ exhibits better high temperature phase stability as Al_2O_3 undergoes several phase transformations (γ-Al_2O_3 to δ-Al_2O_3 to α-Al_2O_3, accompanied with significant volume reduction) under similar conditions. ZrO_2, exists in three different allotropic forms; monoclinic, tetragonal and cubic phases that are stable below ~1100 °C, ~2300 °C, and the melting point respectively. However, on being doped with Y_2O_3 it can occur as tetragonal (partially stabilized ZrO_2) or cubic phase (fully stabilized ZrO_2) at room temperatures. In terms of reactivity with silicate melts, both Al_2O_3, and YSZ are expected to behave similarly (Fig. 2(c) and (d)) [22,24] but in presence of transition elements the former (Al_2O_3) has a tendency to stabilize spinel whose accumulation on the floor of the furnace can clog the draining route and make plant scale operation difficult.

In nature, Al_2O_3 is mostly restricted within silica undersaturated rocks [25,26] and rarely shows any possibility for elemental substitution in its hexagonal structure. In contrast to these, ZrO_2 (baddeleyite) is found to occur within rocks having a wide range of silica saturations [27] and are found to incorporate significant amount of actinides and lanthanides within their cubic fluorite lattice structure. Natural analogue studies as well as available Ellingham diagrams (Fig. 3, [28]) suggest that both Al_2O_3 and ZrO_2 are found to be stable under high temperature and oxidizing conditions. Thus considering the (i) better compatibility with silicate melts, (ii) greater structural flexibility to incorporate actinides and lanthanides, (iii) stability over wide range of temperature-f_{O2} conditions, (iv) lesser tendency to phase transformation and spinel stabilization within borosilicate melts, and (v) excellent leach resistance towards crystal fluids, YSZ is chosen as the preferred coating material over Al_2O_3.

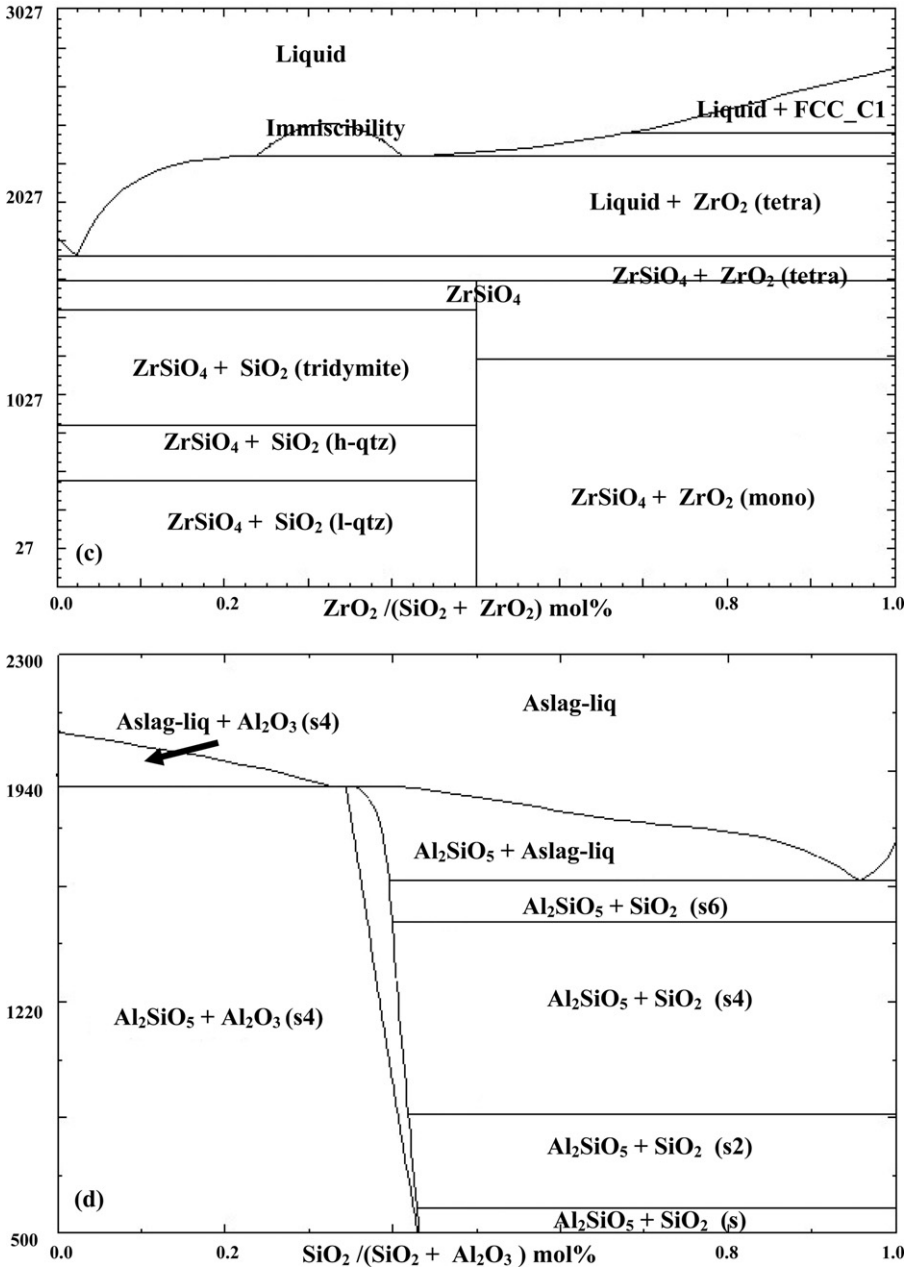

Fig. 2. (*continued*)

4. Identification of the suitable YSZ coating route

Available literatures on 'YSZ coating over metallic substrates' reveal that significant number of attempts have been made with nickel based Superalloys such as Inconel^{TM} 718, Hastelloy^{TM} X, Inconel^{TM} 601, Inconel^{TM} 625, and Inconel^{TM} 738 LC [29–31]. Among the various techniques tried, plasma spray route [17,18,31] is found to yield the best results in terms of excellent thermal, mechanical and chemical properties of the coating, suitable for specific applications in jet engines, gas turbines, diesel engines, etc. However, coatings developed through plasma spray route suffer from porosity and permeability (interconnected porosity), and hence cannot be a good choice as far as 'diffusion barrier application' is concerned. In the present purpose of developing YSZ coating on Alloy 690 is entirely to reduce or nullify any elemental exchange between the alloy and adjacent borosilicate melt. Given these requirements it is proposed to develop YSZ coating in the form of continuous layer on Alloy 690. And to achieve this, a novel synthesis route employing Pulsed Laser Deposition (PLD) technique has been tried in the present case. Detail on the experimental procedure is given below.

5. Experimental procedure

The present study had three important experimental components, namely (a) preparation of coated samples through laying compositionally graded thin films in succession, (b) exposure of coated samples to simulated service conditions and (c) characterizations of blank and exposed samples using microscopic and spectroscopic techniques. Descriptions on each of these aspects are as following.

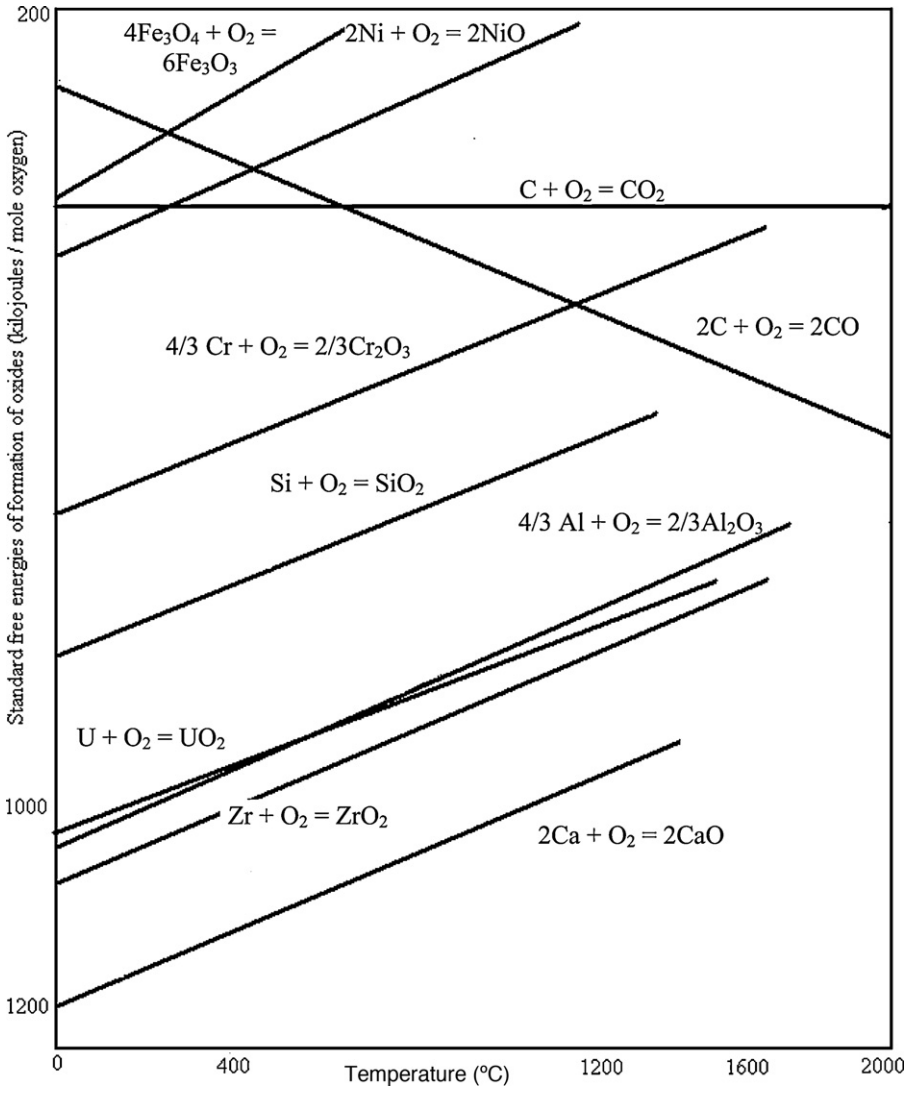

Fig. 3. Schematic Ellingham diagram showing relative positions of selected reactions (modified after Gaskell [28]).

5.1. Preparation of coated samples

The process involved two steps (a) preparation of Alloy 690 coupons and (b) PLD targets. Small coupons (3 mm × 3 mm × 3 mm) of Alloy 690 (Table 1) were obtained from as received mill annealed material and were subsequently prepared for coating through (i) metallographic polishing of the surfaces using different grades of emery papers and fine (1 μm) diamond paste and (ii) at least three times cleaning in ultrasonic bath of ethanol.

The PLD coating source materials, i.e. the targets were prepared by thorough mixing of appropriate amounts of pure (better than 99%) Ni and 9.5 mol% Y_2O_3 stabilized ZrO_2 powders and sintering

Table 1
Compositions of as received Alloy 690 and of phases present in exposed samples.

Element (at%)	Alloy 690 as received	Exposed Alloy 690				Austenitic matrix at glass/coated alloy interface
		Austenitic matrix at glass/alloy interface	Layer (Cr_2O_3)	Needle (Ni_2CrO_4)	Cubic ($NiCr_2O_4$)	
Cr	31.75	27.11	39.07	14.22	23.56	31.92
Fe	9.34	7.82	0.80	0.85	1.30	9.07
Ni	58.91	50.63	0.35	27.71	11.25	55.59
Al	–	–	–	0.45	1.10	–
Si	–	12.61	–	2.07	4.46	–
Zr	–	–	–	–	–	0.42
O	–	–	59.78	54.70	58.33	2.99
Others	C: 0.05 max, Mn: 0.05 max, S: 0.015 max, Si: 0.50 max, Cu: 0.50 max	–	–	–	–	–

Table 2
Composition of coating targets used.

Composition (at%)	Ni80YSZ20	Ni60YSZ40	Ni40YSZ60	Ni20YSZ80	Ni0YSZ100
Ni	40.85	31.30	21.33	10.91	–
Y	1.08	2.21	3.39	4.62	5.91
Zr	5.20	10.62	16.29	22.21	28.41
O	52.87	55.86	58.99	62.26	65.68
Density (gm/cm^3)	8.34	7.78	7.22	6.66	6.10

them at 1400 °C for 8 h in air. To ensure compositional homogeneity, the target materials were crushed and pelletized three times and finally sintered at 1400 °C for 18 h. Five different target materials (e.g. Ni80YSZ20, Ni60YSZ40, Ni40YSZ60, Ni20YSZ80 and Ni0YSZ100; Table 2) were prepared through varying the composition linearly from Ni80YSZ20 to Ni0YSZ100 wt% following the observation of Song et al. [17] who noted that linear feeding of the ingredients produce better coating materials as compared to those obtained from convex or concave feedings. Before use, all targets were metallographically polished, examined with optical microscope and chemically analyzed using Rutherford Backscattering Spectroscopic technique (RBS, described later). In accordance with Ellingham diagram (Fig. 3, [28]) the YSZ component of the targets remained unreduced (metallic Ni can not reduce YSZ as the later is more stable under 1 atmosphere and oxidizing environment) and Ni gained oxygen from the surrounding.

To prevent material degradation in plant scale the required coating thickness will depend on the behavior of the alloy under the service condition, however in the present case, Ni–YSZ composite coatings on the coupons were given in the form of 100–200 nm thin films (in case of thicker coatings, as required for interaction studies, thin films of the same target material were deposited more than

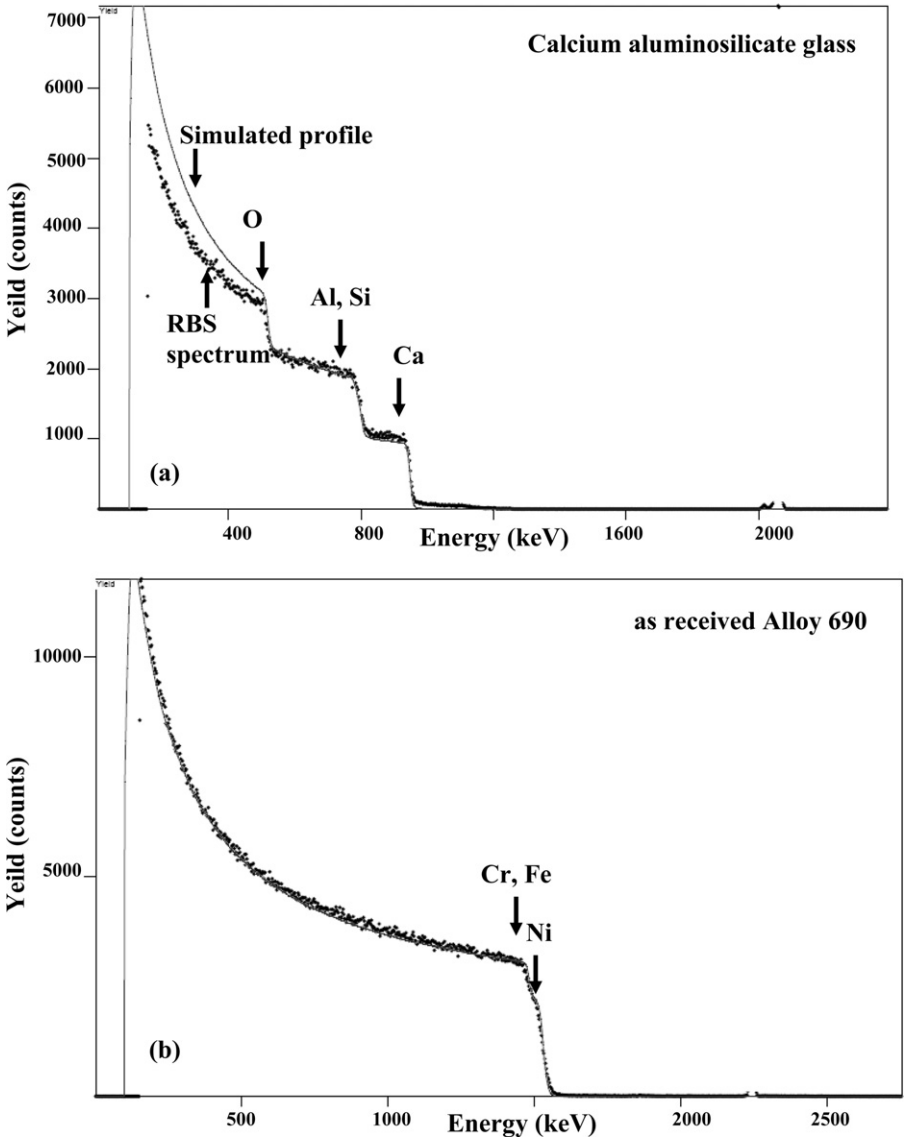

Fig. 4. Representative RBS spectra (indicated by dots) showing the major constituents of (a) calcium borosilicate glass and (b) as received Alloy 690. The grey continuous line represents the fitting curve obtained through simulation of original experimental profile.

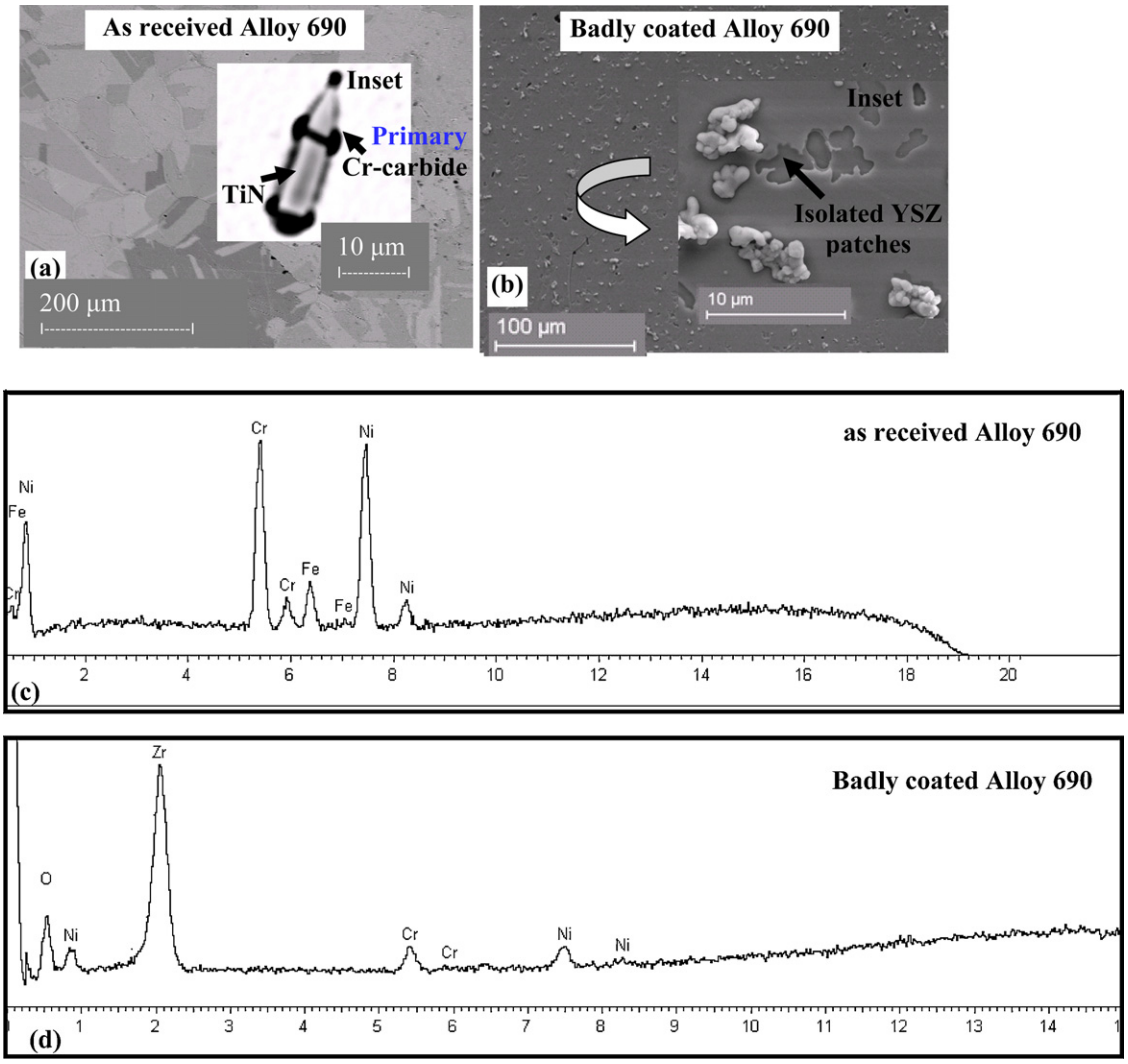

Fig. 5. BSE images showing the representative microstructures of (a) as received Alloy 690 austenitic matrix (inset showing occurrence of Cr-carbide ($Cr_{23}C_6$ type) precipitates surrounding TiN particles within austenitic matrix) and (b) badly coated coupon surface (magnified image is shown in Inset). EDX spectra showing the major constituents of (c) as received Alloy 690 (Ni, Cr and Fe) and (d) isolated white patches (Zr, O with some Ni, Cr) of badly coated sample.

once) so as to carry out all necessary experimental studies within reasonable time frame. The idea was to reduce the experimental time scale through observing the reaction phenomena at a nano-scale level using RBS technique. Before deposition of thin films, the polished substrates were placed on a SiC heater kept inside the PLD chamber maintaining a distance of 40–50 mm from the target. The coupons were initially heated for decontamination and then coated with thin films of desired composition through ablation of rotating targets under vacuum (better than 10^{-6} mbar using a turbo pump) by an excimer Laser (Model LPX 305i from Lambda Physik) of 193 nm wavelength, using ArF gas mixtures [29]. Pulsed laser beams with energies upto 1400 mJ (the actual energy flux at the target surface can be controlled by an aperture or focusing lenses) at a maximum frequency of 50 Hz (pulse duration = 30 ns) were allowed to hit the targets at an angle of 25° and the substrates were placed directly in the path of plasma coming out of the target at right angles to the surface. For rough estimation of the coating thickness, thin film of a given target composition was allowed to deposit on single crystal Si wafer. Mostly, this resulted in generation of concentric color bands with the one having highest interference color at the centre and the lowest one at the periphery. Birefringence of the color bands were obtained by comparing the order of interference color (as seen from Si wafer) with Michael-Levy chart and then dividing it by four times the refractive index of the thin film to obtain a rough thickness of the coating. More accurate coating thickness was obtained from RBS spectrum. For final optimization of the coating thicknesses, the ablation time was varied as it is linearly dependent on the later. For composite coating, the five different targets were ablated in sequence starting with Ni80YSZ20, followed by Ni60YSZ40, Ni40YSZ60, Ni20YSZ80 and Ni0YSZ100. To ensure that coating composition was identical to the target material, thin films were deposited on Si wafer initially and analyzed by RBS technique. In case composition of the coating on Si wafer was different from the target, the same was adjusted by changing the distance between the rotating target and substrate to ensure that the different elemental components of the target did not get separated during its flight in the plasma stream [32]. The coated coupons so obtained were then annealed at 800 °C over 1/2 h within Ni–NiO buffered environment (maintained by a flowing gas mix of CO–CO_2) for (i) stress relaxation and (ii) to ensure good adhesion among the compositionally graded layers and with the substrate.

5.2. Exposure of coated samples to simulated service conditions

To assess the performance of coated Alloy 690 coupons with respect to the uncoated ones, two sets of experiments were

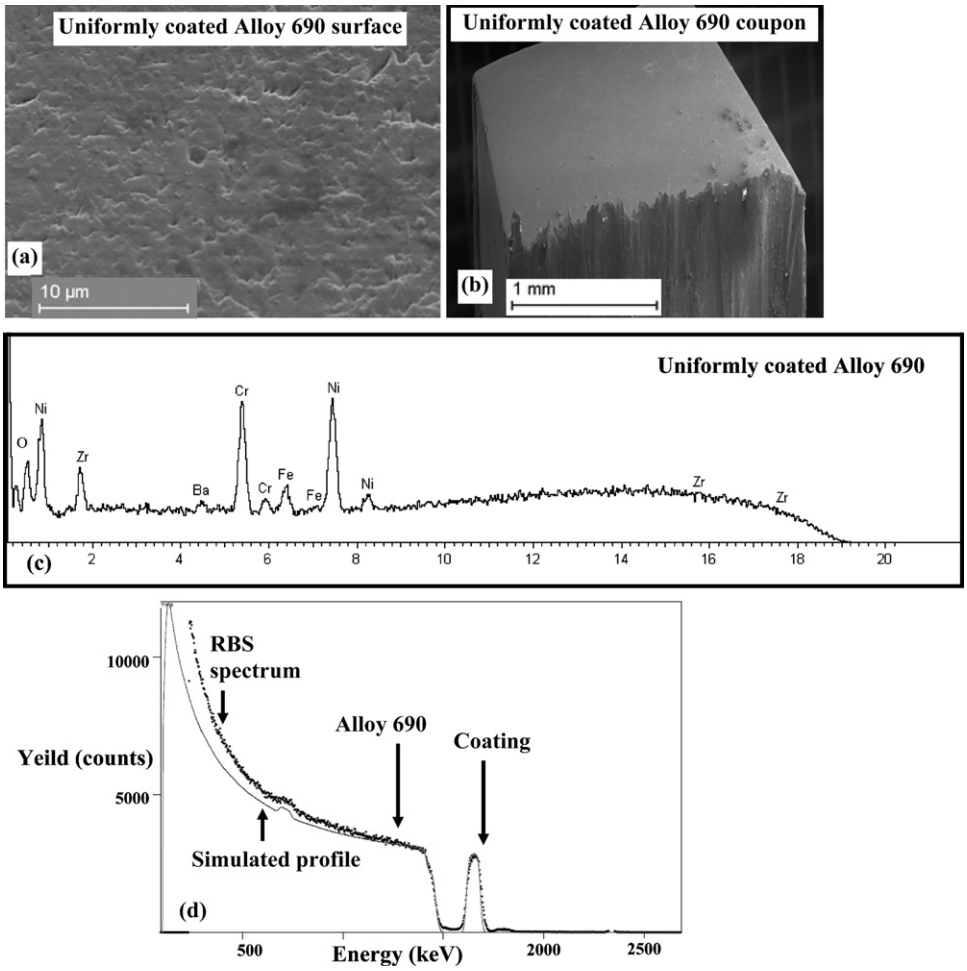

Fig. 6. BSE images showing the compositionally homogeneous and uniformly coated (without any ZrO_2 white patches) Alloy 690 (a) surface and (b) coupon. (c) EDS spectrum shows the major constituents of the coating. (d) RBS spectrum (indicated by dots) of Alloy 690 coupon coated with uniform ~150 nm thick YSZ film. The grey continuous line represents the fitting curve obtained through simulation of original experimental profile.

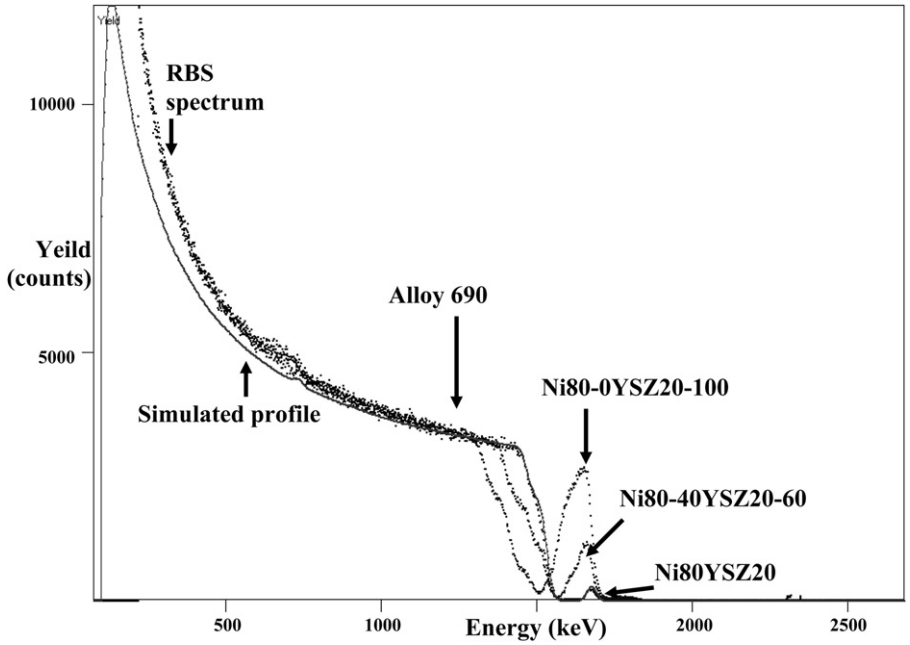

Fig. 7. Overlaid RBS spectra (indicated by dots) showing the stepwise build up of Ni–YSZ composite coating on Alloy 690 substrate. For better clarity fitting curve (grey continuous line) is shown for only one sample (coupon coated with Ni80YSZ20 thin film).

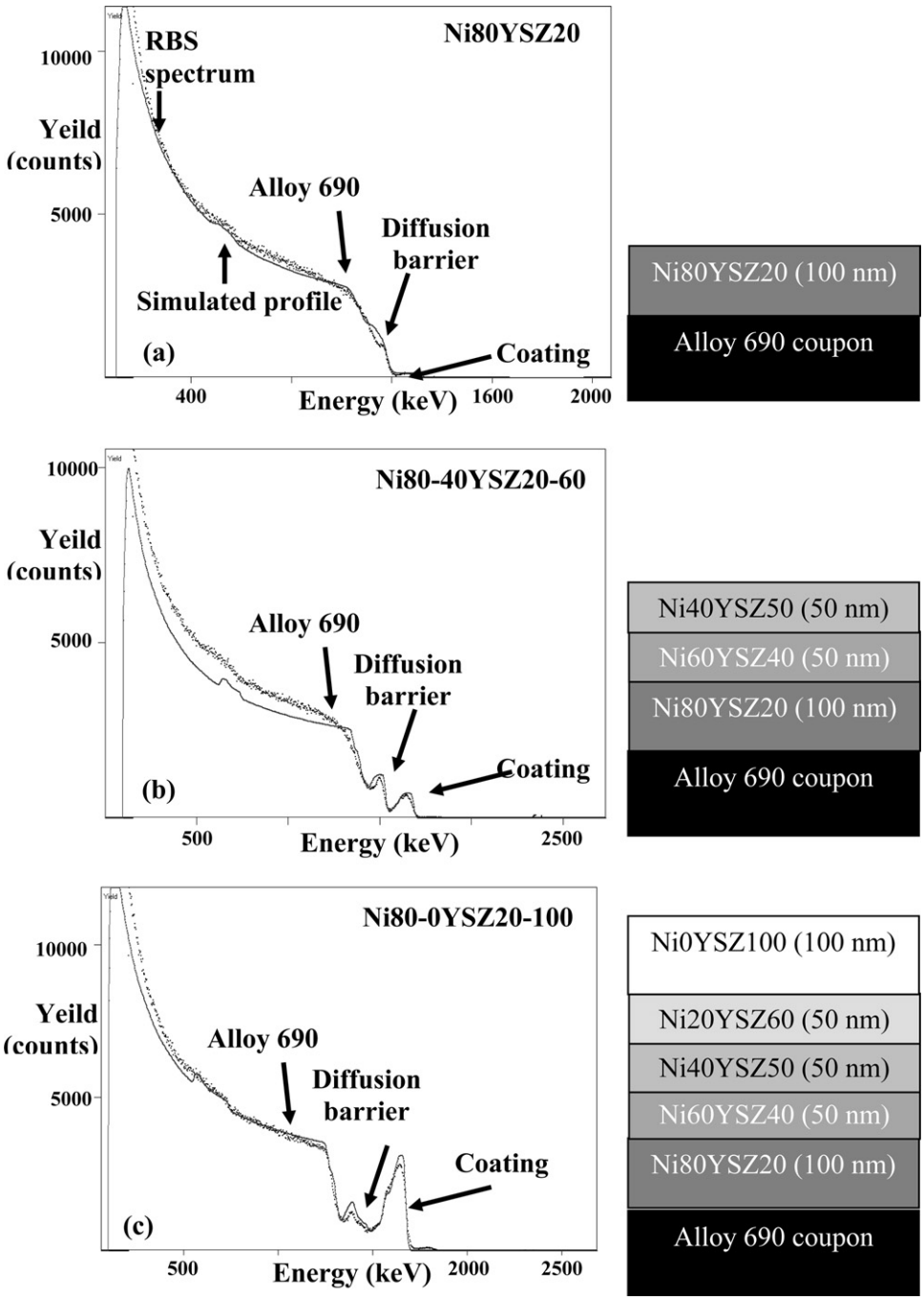

Fig. 8. RBS spectra (indicated by dots) obtained from thermally annealed Alloy 690 coupons coated with (a) Ni80YSZ20, (b) Ni80–40YSZ20–60 and (c) Ni80–0YSZ20–100 Ni–YSZ composite coatings (cartoons showing succession of thin films on Alloy 690 coupon). The fitting curves are marked by grey continuous line.

carried out where coupons were (i) annealed at 1000 °C (temperature maintained within ±1 °C) for 1–6 h within air atmosphere and (ii) exposed to sodium barium borosilicate melt at 1000 °C for 1–6 h. The selection of the experimental conditions was made based on actual plant scale operation procedure where the soaking period and pouring temperature of sodium barium borosilicate melt loaded with HLW are 6 h and 1000 °C respectively [2]. The air-annealing experiments were carried out to simulate the behavior of those Alloy 690 components which do not come in contact with borosilicate melt, e.g. top dish (of metallic melter), upper part of thermowell, feeding channels, etc. On the other hand, the interaction studies between coated/uncoated Alloy 690 coupons with sodium barium borosilicate melt were carried out to understand how coated bottom dish (only in case of metallic melter), electrodes, pour spout assembly, etc. may respond to it. In these experiments coupons were put inside Pt crucibles containing sodium barium borosilicate glass powders (prepared through conventional melt-quench route [2]) and annealed for the above mentioned pre-determined time–temperature schedule within air atmosphere furnace. The glass composition was chosen to be sodium barium borosilicate because this is being produced at Waste Immobilization Plant, Trombay (India) for immobilization of its sulfate rich HLW [2].

5.3. Sample characterization

A three stage characterization strategy, involving (a) optical microscopy, (b) Rutherford Backscattering Spectroscopy (RBS)

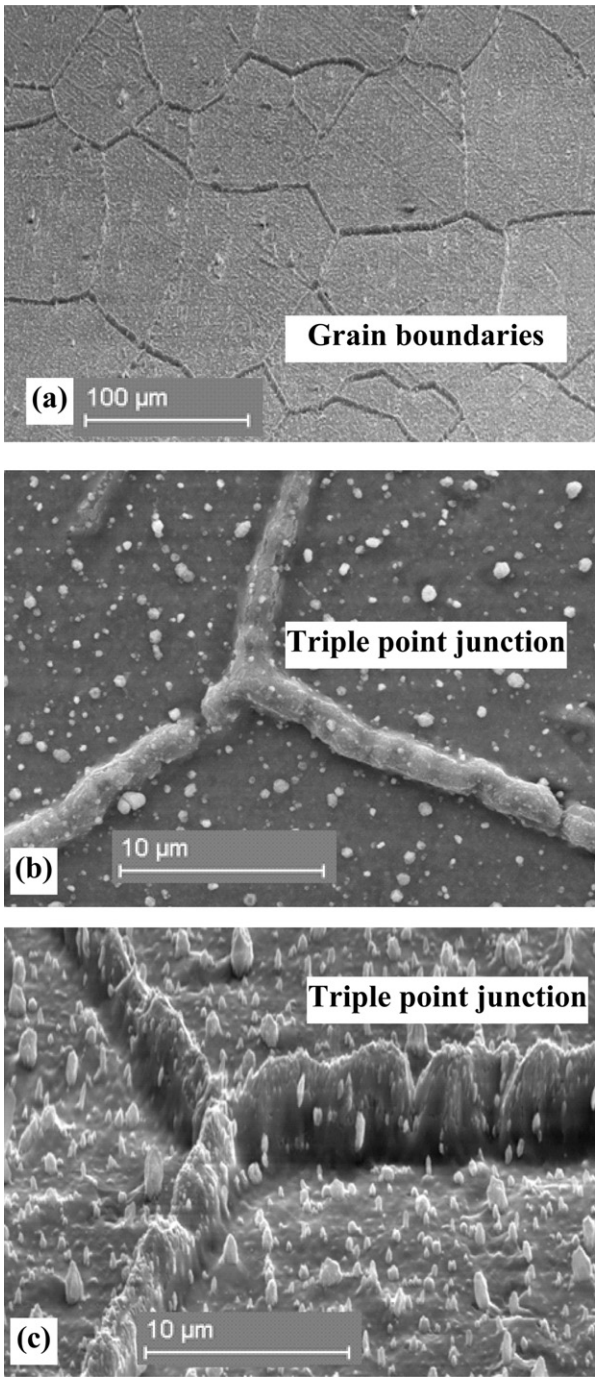

Fig. 9. BSE images showing the growth of YSZ coating upon thermal annealing.

and (c) Scanning Electron Microscopy (SEM; Cambridge Stereoscan) along with micro-chemical analysis using Energy Dispersive Spectrometers (EDS; Oxford EDS) were adopted in the present investigation.

All samples including blanks were studied under reflected light in an optical microscope for preliminary microstructural characterizations.

For RBS analyses, the Dynamitron Tandem Accelerator Facility of the Ruhr University Bochum was used to analyze the thermally annealed samples and blanks. The technique, which is essentially a depth resolved mass spectrometry of near surface layers (depth <0.5 μm), is based on the measurement of the energies of light ions accelerated by high voltage that have been scattered back elastically from the constituent atoms of a given sample. Monoenergetic (2 MeV) beams of alpha particles (^{4}He), produced in the linear accelerator, collimated to a diameter of 0.5 mm, were allowed to impinge on the sample and those scattered back from it were detected on a Si particle detector at a backscattering angle of 170°. For each sample, spectra of particle yields as a function of energy were documented by a multichannel analyzer (MCA). It may be mentioned here that the energy of the detected ions depends upon the mass of the target atoms and the depth within the material at which they are located. For a thick (few hundreds of nanometers or above) multi-component sample, the energy spectrum is the sum of contributions from each constituent atom. Hence a typical RBS spectrum is usually constituted of a series of steps whose edges correspond to scattering events at the sample surface and the corresponding energy bears the identity of the atoms present. As an example, RBS spectrum obtained from calcium aluminosilicate glass is shown in Fig. 4(a). Note that depending on energy distributions elements may have separated (e.g. O, Ca) or overlapping (Al, Si) peak positions. The latter is specifically important for the materials used in the present study, i.e. Alloy 690 (very close peak positions for Ni, Fe and Cr; Fig. 4(b)) and YSZ (very close peak positions for Zr and Y). It may be added here that particles with lower energies (when considering only scattering events due to a particular atom in the sample) result from scattering at depth in the material, as the ingoing (before scattering) and outgoing (after scattering) ions lose energy as they travel through it. The number of detected ions at a given energy is directly related to the concentration of the atomic species and the probability of a scattering event occurring. The latter factor is proportional to the square of the atomic number (Z) of the target atom, resulting in greater detection sensitivity for high-Z atoms. The RBS spectra so obtained were fitted and analyzed by RBX software [33], feeding the required input parameters such as compositions (coatings and substrate), coating thickness, and coating density (Table 2). The particle yields were converted to concentrations by taking into account the probabilities of scattering events for a given atomic species at various depths in the sample.

Samples exposed to borosilicate melts were analyzed using SEM-EDX. One side of the samples was metallographically polished to remove adhering borosilicate glass so as to examine the Alloy 690-coated-borosilicate glass cross-sections. The polished cross-sections were subsequently coated with thin conducting carbon film for microstructural characterization with a steady electron beam of 4 nA, accelerated under 20 keV voltage. For energy based element identification, liquid N_2 cooled Si–Li detector was used and for concentration estimations raw data were corrected for atomic number (Z), absorption (A) and fluorescence (F) following PAP procedure [34]. Detailed investigations on the samples were carried out under scanning and static beam modes and the results are described below.

6. Results and discussion

Microstructural characterization of 'as received' Alloy 690 material shows the presence of tiny TiN inclusions and primary Cr carbide precipitates within the γ-austenitic matrix [14] with an average grain size of ~80 μm (Fig. 5(a)). On such Alloy 690 coupons five layer composite thin films of Ni–YSZ were deposited using PLD technique. During initial trial stage with Ni0YSZ100 target, presence of (i) white patches, (ii) wrinkles and (iii) cracks were found within the thin-films (Fig. 5(b)). Microchemical analyses of the coupon indicate Ni, Cr and Fe as the major constituents of Alloy 690 (Fig. 5(c)) and those of white patches identify them as ZrO_2 with marginal amount of Ni and Cr within it (Fig. 5(d)) and subsequently the experimental parameters (energy and frequency of the laser, time of coating, etc.) were optimized to obtain compositionally homogeneous (without any white patches), pore free, uniform

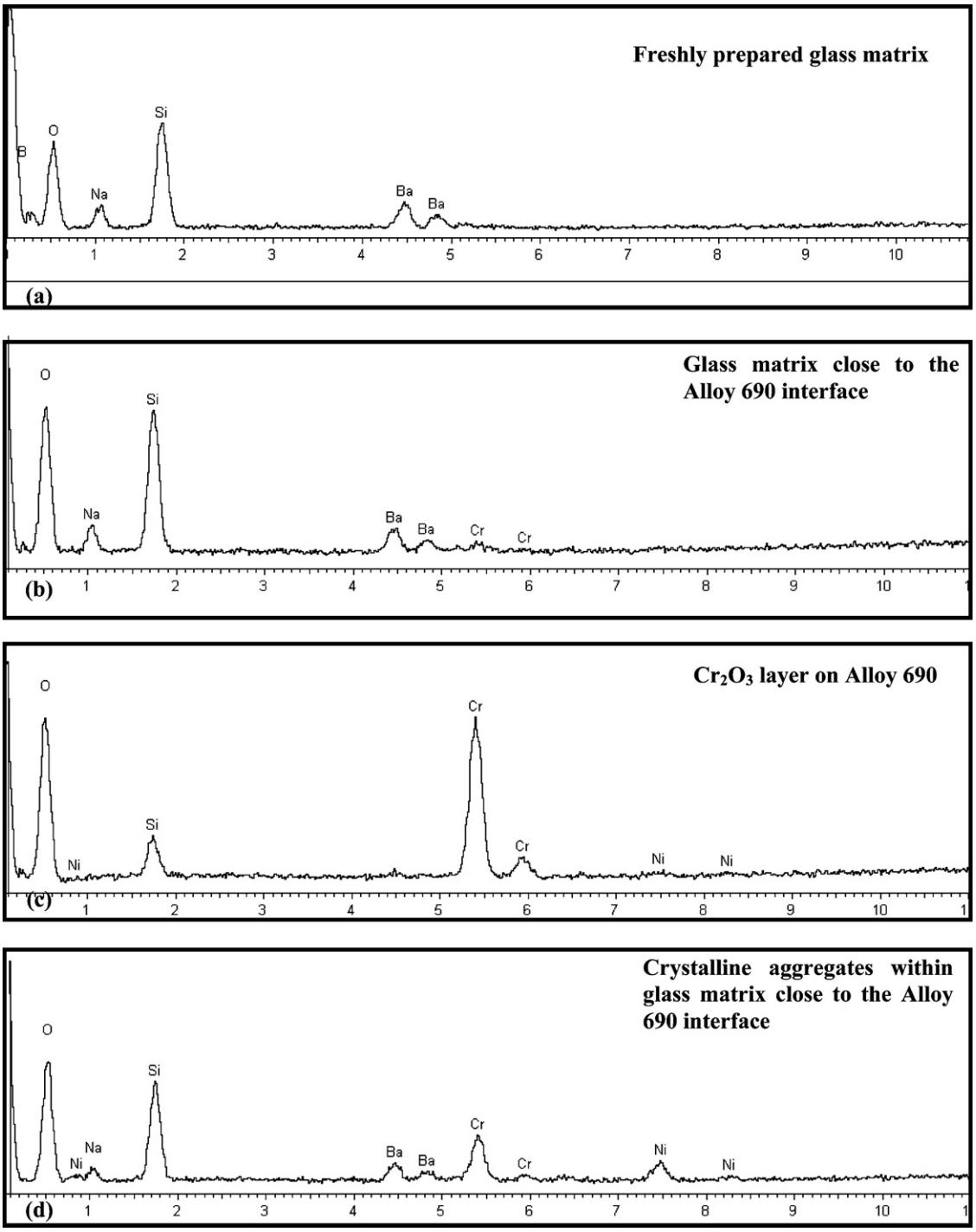

Fig. 10. EDX spectra showing the major constituents of various samples.

composite coating on the Alloy 690 substrate (Fig. 6(a) and (b)). To check compositional homogeneity, X-ray energy and Rutherford Backscattered particle spectra were taken from multiple places on the coating and the representative data are shown in Fig. 6(c) and (d). Analysis of the RBS spectrum (Fig. 6(d)) using fitting parameters such as possible composition, thickness, and density indicate that the overall coating thickness for the sample under description was ~150 nm and the top layer was essentially YSZ. EDS spectrum (Fig. 6(c)) however indicated that besides Zr and O; Ni, Cr and Fe are also present within the coating. The difference in the compositions for the same coating material is essentially linked to the variations in the X-ray/back scattered particle–interaction volumes. While for RBS technique the signal is collected from top few tens of nanometer, but for EDS it is usually few hundreds of nanometer (considering the beam conditions used in the present study). Hence it is believed that the presence of Ni, Cr and Fe peak within the EDS spectrum (Fig. 6(c)) are essentially due to Alloy 690 substrate. Preliminary 'Electron Back Scatter Diffraction (EBSD)' study identifies that all the five layers of the composite coatings are crystalline in nature.

As mentioned earlier, on the Alloy 690 coupon, five layers of Ni–YSZ composite coating was built up in a stepwise manner as shown in Figs. 7 and 8. Note that in Fig. 7 the variation in yields (Y-axis) is due to variation in overall coating thickness. For equally thick coating the yields were found to be comparable. The excel-

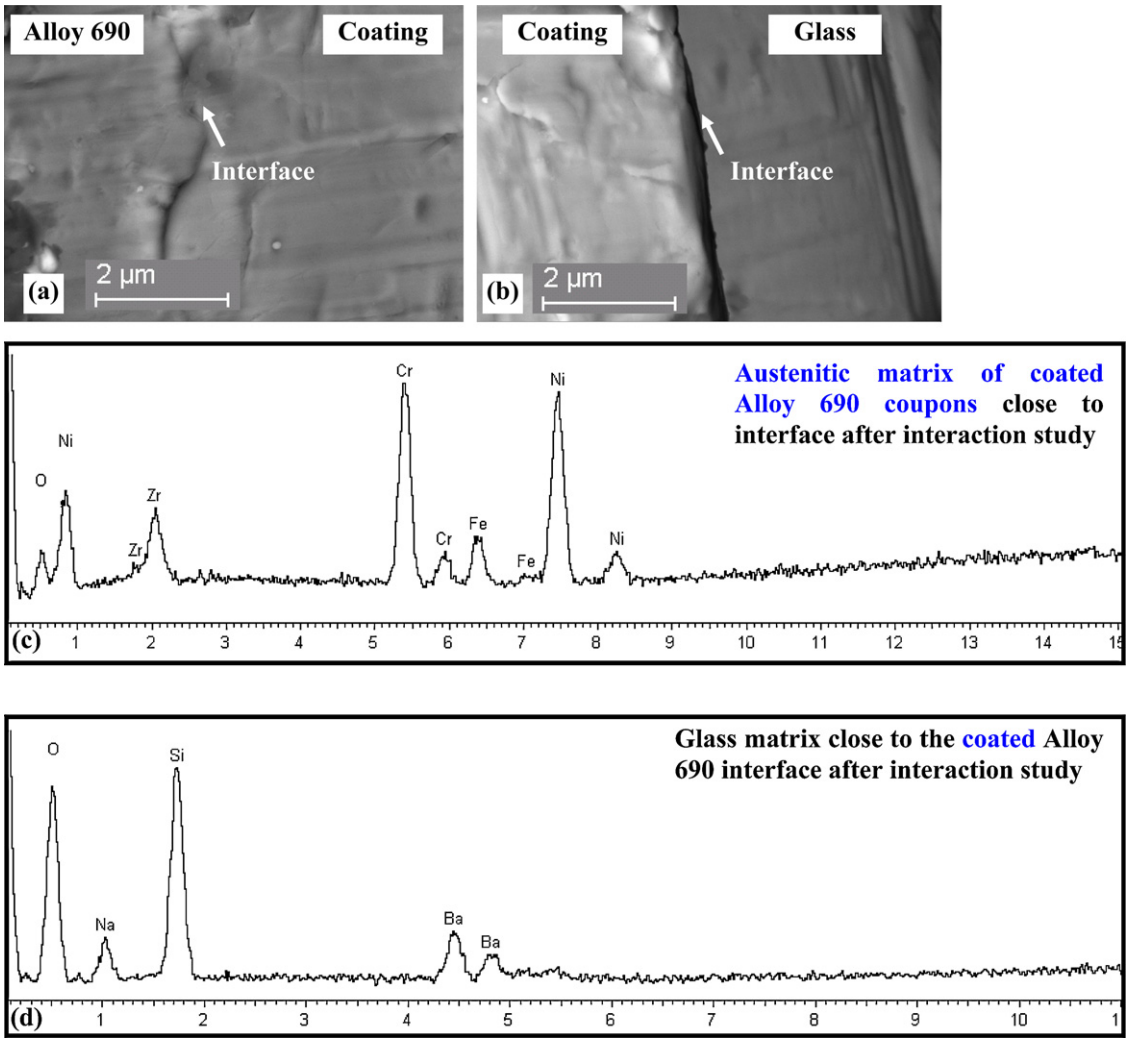

Fig. 11. BSE images showing (a) good contact relationship (no pore, gap or crack at the interface) between compositionally graded layer and Alloy 690 substrate and (b) formation of no reaction product at the coating/melt interface even after an exposure to sodium borosilicate melt at 1000 °C for 2 h. (c) EDX spectra showing the major constituents of the (c) Alloy 690 close and (d) the glass matrix close to interface after interaction study.

lent fitting of the raw data, for this as well as for other spectra, suggest that compositions of target pellets were maintained in corresponding thin films in each case. Fig. 8(a)–(c) show the RBS spectra obtained from the same set of samples mentioned in Fig. 7 after annealing in air at 1000 °C for 6 h. Compositional analyses of the Alloy 690–Ni80YSZ20 interfaces (using the RBS spectrum) show (a) absence of any Cr-oxides (Cr_2O_3, $NiCr_2O_4$ and Ni_2CrO_4) and (b) increase in Cr content (from 0 to 12 at%) within the composite coat. These are very important observations as they indicate that the Ni80YSZ20 composite layer was impermeable enough to prevent or significantly reduce oxygen ingress from the air atmosphere towards the alloy substrate. Given the high oxygen self diffusion coefficient (of the order of $\sim 10^{-10}$ m^2/s) [35,36] of YSZ under the experimental conditions, the possible reason behind such inertness could be diffusion of Ni within YSZ. The moderate diffusivity of Ni within YSZ ($\sim 10^{-20}$ m^2/s) [37] under the experimental conditions, and the experimentally proven fact that oxygen conductivity and diffusivity within ZrO_2 reduce significantly as the Y_2O_3 content goes down below 8 mol% [38] substantiate our reasoning. Enhancement of Cr within Ni–YSZ composite coating was due to diffusion out of the former in minor quantity from alloy substrate. Detailed spectra analyses of all other annealed samples highlight the same observations. The peaks occurring in between the alloy substrates and coatings (Fig. 8(a)–(c)) are nothing but the Cr rich domains of the Ni80YSZ20 composite coatings mentioned earlier. It may be mentioned here that in all annealed samples no trace of any discontinuity (pore, crack, and scale formation) was observed at the alloy–coat interfaces. The YSZ coating, however, found to grow upon thermal annealing, and this was maximum at the grain boundaries probably due to easier mass transfer (Fig. 9(a)–(c)). Further, composition of the austenitic matrix (adjacent to the coating) within annealed coated samples was found to be very similar to the 'as received material' (Table 1).

Similar encouraging results were obtained from coupon-borosilicate melt interaction studies also. It was noted that uncoated Alloy 690 coupons on being exposed to sodium barium borosilicate melt at 1000 °C for 2 h: (i) gave rise to Cr_2O_3 layer, (ii) crystallized and grew needle and cubic shaped phases and (iii) significant Cr depletion took place from the austenitic matrix (Figs. 1(b), 10(c) and (d); Table 1). (iv) An increase in Cr content (as high as 7.64 at%) within the glass matrix close to the coupon melt interface was also noted (Fig. 10(a) and (b)). Interestingly, in contrary to these, no compositional modifications could be witnessed in case of coated Alloy 690 coupons exposed to sodium barium borosilicate melt at 1000 °C for 2 h (Fig. 11(a)–(d)). Microchemical analyses of Alloy 690 or glass matrix close to interfaces showed more or less same compositions as those measured far away from the

interface. Hence this suggests that the proposed Ni–YSZ compositionally graded coating can protect corrosion of Alloy 690 components from borosilicate melt.

The success of 'compositionally graded coating' as 'diffusion barrier' in the present context is essentially keyed to restricted mass transfer mechanisms. Coating of as received Alloy 690 coupons with Ni80YSZ20 thin films and subsequent annealing under low f_{O2} (Ni–NiO buffer) conditions arrested Cr out-flux from Alloy substrate to coating as Ni and Cr have no mutual solubility. Subsequently, gradual variations in thin film compositions eliminated the possibility of any reaction product formation through out the coating. Finally, the inert nature of YSZ thin film protected the underlying coating and Alloy 690 coupon from sodium barium borosilicate melt corrosion.

In fine, it can be argued that the proposed five layered Ni–YSZ compositionally graded composite coating stands a good chance to qualify as a 'chemical diffusion barrier' coating material for Alloy 690 components used in HLW vitrification furnaces. However the coating thickness used in the present investigation is much smaller than what is actually required in practice. So there is a need to scale up the coating thickness and repeat the experiments once again. Moreover there are considerable chances to improve upon the composite coating material through incorporation of YSZ containing more than 10 mol% Y_2O_3 as in such case the inherent oxygen diffusivity of the material is expected to be less [38]. Once this is done there is a need to assess the composite coating materials in terms of its thermal conductivity, high temperature fatigue, bond strength, response to thermal cycling, etc. Efforts in these directions have already been initiated and the experimental results will be published elsewhere.

7. Summary

(i) Homogeneous, uniform, pore free, five layered compositionally graded Ni–YSZ composite coating can be developed over Alloy 690 substrate using PLD technique.

(ii) The graded composite coating can arrest development of mixed oxide layer (Cr_2O_3, $NiCr_2O_4$ and Ni_2CrO_4) on Alloy 690 surface due to its exposure to high temperature-oxidation conditions.

(iii) The graded composite coating can control Cr depletion from Alloy 690 matrix and formation of crystalline aggregates within waste glass due to borosilicate melt-Alloy 690 interactions.

(iv) Hence, the compositionally graded five layered Ni–YSZ composite coating, developed via PLD route, stands a good chance to qualify as a diffusion barrier coating material for Alloy 690 components used in HLW vitrification furnaces.

Acknowledgements

Pranesh Sengupta acknowledges Alexander von Humboldt Foundation for financial support. The authors are grateful to the reviewers for their constructive comments and to Dr. G. Li Puma for carrying out the Editorial responsibility.

References

[1] M.I. Ojovan, W.E. Lee, New Developments in Glassy Nuclear Wasteforms, Nova Science Publishers, 2007.
[2] C.P. Kaushik, R.K. Mishra, P. Sengupta, D. Das, G.B. Kale, K. Raj, Barium borosilicate glass: a potential matrix for immobilization of sulfate bearing high level radioactive waste, J. Nucl. Mater. 358 (2006) 129–138.
[3] R.K. Mishra, P. Sengupta, C.P. Kaushik, A.K. Tyagi, G.B. Kale, K. Raj, Studies on immobilization of thorium in barium borosilicate glass, J. Nucl. Mater. 360 (2007) 143–150.
[4] R.K. Mishra, V. Sudarsan, P. Sengupta, R.K. Vatsa, A.K. Tyagi, C.P. Kaushik, D. Das, K. Raj, Role of sulphate in structural modifications of sodium barium borosilicate glasses developed for nuclear waste immobilization, J. Am. Ceram. Soc. 91 (2008) 3903–3907.
[5] P. Sengupta, S. Fanara, S. Chakraborty, Preliminary study on calcium aluminosilicate glass as a potential host matrix for radioactive ^{90}Sr – an approach based on natural analogue study, J. Hazard. Mater. 190 (2011) 229–239.
[6] US Department of Energy, Waste Vitrification Systems lessons learned, vol. 62, US Department of Energy, Germantown, 1999.
[7] K. Raj, K.K. Prasad, N.K. Bansal, Radioactive waste management practices in India, Nucl. Eng. Des. 236 (2006) 914–930.
[8] P. Mishra, P. Sengupta, S.N. Athavale, A.L. Pappachan, A.K. Grover, A.K. Suri, G.B. Kale, P.K. De, K. Bhanumurthy, Brazing of HIP-Al_2O_3 to stainless steel (AISI 304L) by Mo–Mn route using 72Ag–28Cu braze, Metal. Mater. Trans. 36A (2005) 1075–1084.
[9] P. Sengupta, Interaction study between nuclear waste glass melt and ceramic melter bellow liner materials, J. Nucl. Mater. 411 (2011) 181–184.
[10] V. Kain, P. Sengupta, P.K. De, S. Banerjee, Case reviews on the effect of microstructure on the corrosion behavior of austenitic alloys for processing and storage of nuclear waste, Metal. Mater. Trans. 36A (2005) 1075–1084.
[11] P. Sengupta, J. Mittra, G.B. Kale, Interaction between borosilicate melt and Inconel, J. Nucl. Mater. 350 (2006) 66–73.
[12] P. Sengupta, C.P. Kaushik, R.K. Mishra, G.B. Kale, Microstructural characterization and role of glassy layer developed on process pot wall during nuclear high-level waste vitrification process, J. Am. Ceram. Soc. 90 (2007) 3085–3090.
[13] P. Sengupta, N. Soudamini, C.P. Kaushik, R.K. Mishra, D. Das, G.B. Jagannath, K. Kale, B.P. Raj, Sharma, Corrosion of alloy 690 process pot by sulfate containing high level radioactive waste at feed stage, J. Nucl. Mater. 374 (2008) 185–191.
[14] P. Sengupta, C.P. Kaushik, G.B. Kale, D. Das, K. Raj, B.P. Sharma, Evaluation of Alloy 690 process pot at the contact with borosilicate melt pool during vitrification of high level nuclear waste, J. Nucl. Mater. 392 (2009) 379–385.
[15] K.J. Imrich, D.F. Bickford, G.G. Wicks, R.C. Hopkins, Resistance of materials at elevated temperatures to the adherence of molten borosilicate glass, Ceram. Trans. 107 (2000) 384–390.
[16] D.F. Bickford, A. Applewhiteramsey, C.M. Jantzen, Control of radioactive waste glass melters. 1. Preliminary general limits at Savanah River, J. Am. Ceram. Soc. 73 (1990) 2896–2902.
[17] Y.S. Song, I.G. Lee, D.Y. Lee, D.J. Kim, S. Kim, K. Lee, High temperature properties of plasma sprayed coatings of YSZ/NiCrAlY on Inconel substrate, Mater. Sci. Eng. A 332 (2002) 129–133.
[18] Z.L. Dong, K.A. Khor, Y.W. Gu, Microstructure formation in plasma sprayed functionally graded NiCoCrAlY/Yttria stabilized zirconia coatings, Surf. Coat. Technol. 114 (1999) 181–186.
[19] A.M. Khoddami, A. Sabour, S.M.M. Hadavi, Microstructure formation in thermally sprayed duplex and functionally graded NiCrAlY/Yttria Stabilized Zirconia coatings, Surf. Coat. Tech. 201 (2007) 6019–6024.
[20] Y.J. Su, R.W. Trice, K.T. Faber, H. Wang, W.D. Porter, Thermal conductivity, phase stability and oxidation resistance of $Y_3Al_5O_{12}$ (YAG)/Y_2O_3–ZrO_2 (YSZ) thermal barrier coatings, Oxid. Met. 61 (2004) 253–271.
[21] B. Ferrari, R. Moreno, Ni–YSZ graded coatings produced by dipping, Adv. Eng. Mater. 6 (2004) 969–971.
[22] FACTSAGE, Facility for the Analysis of Chemical Thermodynamics software, 2009.
[23] T.M. Besmann, N.S. Kulkarni, Thermochemical analysis and modelling of the Al_2O_3–Cr_2O_3, Cr_2O_3–SiO_2, and Al_2O_3–Cr_2O_3–SiO_2 systems relevant to refractories, J. Am. Ceram. Soc. 89 (2006) 638–644.
[24] V. Frishfelds, A. Jakovics, A. Muehlbauer, B. Nacke, Dynamic of incongruent melting of ZrO_2–SiO_2 in inductor crucible, in: International Scientific Colloquium, Modeling for Material Processing, Riga, June 8–9, 2006, pp. 149–154.
[25] V.A. Pakhomova, B.L. Zalishchak, E.G. Odarichenko, M.I. Lapina, N.S. Karmanov, Study of melt inclusions in the Nezametnoye corundum deposit, Primorsky region of the Russian Far East: petrogenetic consequences, J. Geochem. Explor. 89 (2006) 302–305.
[26] T. Morishita, S. Arai, Petrogenesis of corundum bearing mafic rock in the Horoman Peridotite Complex, Japan, J. Petrol. 42 (2001) 1279–1299.
[27] T.B. Bayanova, Baddeleyite: a promising geochronometer for alkaline and basic magmatism, J. Petrol. 14 (2006) 187–200.
[28] D.R. Gaskell, Introduction to Metallurgical Thermodynamics, second ed., McGraw-Hill Book Company, 1981, p. 287.
[29] M. Saremi, A. Afrasiabi, A. Kobayashi, Microstructural analysis of YSZ and YSZ/Al_2O_3 plasma sprayed thermal barrier coatings after high temperature oxidation, Surf. Coat. Technol. 202 (2008) 3233–3238.
[30] T. Niki, K. Ogawa, T. Shoji, Mechanical and high temperature oxidation properties of cold sprayed CoNiCrAlY coatings for thermal barrier coating, J. Solid Mech. Mater. Eng. 2 (2008) 739–747.
[31] A.M. Khoddami, A. Sabour, S.M.M. Hadavi, Microstructure formation in thermally sprayed duplex and functionally graded NiCrAlY/Yttria stabilized zirconia coatings, Surf. Coat. Technol. 201 (2007) 6019–6024.
[32] R. Dohmen, H.W. Becker, E. Meissner, T. Etzel, S. Chakraborty, Production of silicate thin films using pulsed laser deposition (PLD) and applications to studies in mineral kinetics, Eur. J. Mineral. (2002) 1155–1168.
[33] E. Kotai, Computational methods for analysis and simulation of RBS and ERDA spectra, Nucl. Instr. Meth. B 85 (1994) 588–596.
[34] J.L. Poucho, F. Pichoir, Determination of mass absorption coefficients for soft X-rays by use of the Electron Microprobe, in: D.E. Newbury (Ed.), Microbeam Analysis, San Francisco Press, California, 1988, pp. 319–324.

[35] K. Suzuki, A. Endou, R. Miura, Y. Oumi, H. Takaba, M. Kubo, A. Chatterjee, A. Fahmi, A. Miyamote, Molecular dynamics simulations on oxygen ion diffusion in strained YSZ/CeO_2 superlattice, Appl. Surf. Sci. 130–32 (1998) 545–548.
[36] H.W. Brinkman, W.J. Briels, H. Verweij, Molecular dynamics simulations of yttria-stabilized zirconia, Chem. Phys. Lett. 247 (1995) 386–390.
[37] C. Argirusis, M.A. Taylor, M. Kilo, G. Borchardt, F. Jomard, B. Lesage, O. Kaitasov, SIMS study of transition metal transport in single crystalline yttria stabilized zirconia, Phys. Chem. Chem. Phys. 6 (2004) 3650–3653.
[38] M. Kilo, C. Fundenberger, H. Argirusis, M.A. Taylor, G. Borchardt, M. Weller, R. Jackson, Experimental and theoretical investigation of oxygen diffusion in stabilized zirconia, Radiat. Eff. Defects Solids 157 (2002) 1077–1083.